

Drone-based impact-echo inspection system for non-destructive testing of concrete structures

Claudia Thurnherr ^{*}, Aurélia Muller, Daniel Algernon

Laboratory for Non-Destructive Evaluation, SVTI - Swiss Association for Technical Inspections, Richtistrasse 15, Wallisellen CH-8304, Switzerland



ARTICLE INFO

Keywords:

Drone-based inspections
Impact-echo
Non-destructive testing

ABSTRACT

Drones have been cited as a key technology to improve the efficiency and effectiveness of non-destructive testing (NDT). In particular, bridges, containments, or cooling towers are the focus of drone-based structural inspections due to the risks associated with their aging structure and limited accessibility. In this study, the objectives of structural health assessment are the detection of defects such as flaws or delaminations in concrete and the measurement of geometrical properties such as wall thicknesses. The impact-echo method is an NDT technique based on elastic wave properties that can characterize such defects. The development of a drone-based impact-echo measurement sensor unit was achieved through a drone platform that allows the application of a contact force in almost any orientation. The sensor unit contains an automated impactor and a contact sensor. The coupling between a structure's region of interest and the sensor is achieved through a newly designed sensor holder. This paper presents respectively the concept and the design of the sensor unit and its integration on the drone. Furthermore, the results of an in-flight inspection test using a reference concrete block containing a tendon duct as well as delamination are reported. These results demonstrate the feasibility of the drone-based impact-echo system. The developed sensor unit can be used in the future for structural diagnostics and to ensure healthy infrastructure.

1. Introduction

Structural diagnostics and durability assessment are crucial topics for the preservation of ageing concrete infrastructures. Defects can be introduced into a structure during its construction or its service life. Hence, reliable tools are needed to detect these imperfections before their size reaches a critical threshold that could jeopardize the structural integrity and the safe use of the infrastructure. Non-Destructive Testing (NDT), also known as Non-Destructive Evaluation (NDE) or Non-Destructive Inspection (NDI), deals with methodologies for the non-destructive assessment of materials, structures, or systems for both manufacturing and in-service inspections. These techniques can be used to detect and size defects, which is crucial for repair decisions. NDT can also be used to assess the constructive design of infrastructure, such as rebar detection, localization, and sizing.

Various NDT measurement techniques are commercially available for engineers to inspect concrete infrastructure in civil engineering [17, 29,3]. Advanced NDT provides the ability to inspect the internal condition of a structure, going beyond what is visible from the outside.

Unlike standard visual inspections, which only assess surface-level defects, advanced NDT techniques allow for deeper analysis by detecting subsurface flaws, material inconsistencies, and structural weaknesses. These methods enable a more comprehensive assessment of a component's integrity without causing damage, making them invaluable for civil engineering where safety and reliability are critical. Advanced NDT is often contact-based, meaning the testing equipment must be in direct or near-direct interaction with the material being inspected. Such NDT methods for concrete structures commonly include ground-penetrating radar (GPR), ultrasonics, and impact-echo. Each technique is underpinned by distinct physical principles, enabling specific applications and addressing unique aspects of material evaluation and structural assessment [28]. GPR operates on the propagation of electromagnetic waves and is frequently employed for rebar detection due to its sensitivity to variations in dielectric properties. In contrast, both ultrasonics and impact-echo techniques rely on the propagation of mechanical (or elastic) waves, making them particularly sensitive to acoustic boundaries and well-suited for the detection of voids, delaminations, and back-wall reflections. These NDT methods are complementary, each

* Corresponding author.

E-mail addresses: claudia.thurnherr@svti.ch (C. Thurnherr), aurelia.muller@svti.ch (A. Muller), daniel.algernon@svti.ch (D. Algernon).

offering unique insights into the material properties and potential defects within concrete structures, thereby enhancing the overall integrity assessment process [38]. A key challenge in NDT for civil engineering is accessibility, as inspections often require scaffolding or other costly and time-consuming infrastructure to reach high or difficult-to-access areas. This limitation can be effectively overcome by drone-based approaches, which enable efficient and safe inspections without the need for extensive support structures. However, one of the primary challenges in developing a drone-based NDT system is the stringent design limitations imposed by the drone itself, including constraints on weight, power supply, and data processing capacity. These factors must be carefully balanced to ensure the feasibility and effectiveness of drone-assisted inspections. Ultimately, these factors collectively influence the selection of the appropriate NDT method, as the inspection system must align with the operational capabilities of the drone while maintaining reliability and accuracy. In this study, impact-echo was selected due to its potential to benefit significantly from automation of the data acquisition process. Additionally, it is relatively lightweight when using a single probe and has modest energy requirements, making it an ideal choice for drone-based NDT applications.

The impact-echo method is an NDT technique where elastic stress waves are excited in the inspected structure with an impact point using a hammer or a steel ball. Following the impact, a local resonance mode related to the layer thickness is measured and analyzed in the frequency domain with a probe near the impact source. It was first introduced in 1986 [40] and has become a common inspection method for concrete structures. In particular, impact-echo is applied to assess the construction quality and current condition of transportation structures, such as bridges and tunnels [46], as well as concrete structures in the energy sector, such as for the structural assessment of containments in nuclear power plants [25] or for the inspection of concrete dams in hydropower plants ([31]). Recently, a study was published where impact-echo was used for defect detection in sandwich composites for the assessment of wind turbines [21]. The impact-echo technique can be used to measure wall thicknesses [41], to find defects such as flaws or delaminations in concrete [7], or to inspect the grout quality of tendon ducts [18,50] in prestressed structures. The method is also often used to determine the sound velocity in the material from a known wall thickness or vice versa [8]. The relation between the measured frequency f and the wall thickness d is hereby given as the following equation:

$$f = \frac{\beta \cdot c_L}{2 \cdot d} \quad (1)$$

where β represents the correction factor (often found to be 0.96 and analyzed in detail in [14]) and c_L refers to the speed of sound of the longitudinal wave. Typically, the impact-echo method is applied as a grid measurement with successive impacts and measurement points and evaluated through imaging [51]. The waveform signal is acquired on each grid point in the time domain; for analysis, the waveform is then transformed into the frequency domain using a Fast Fourier Transformation (FFT). The layer thickness resonance is identified using the dominant frequency in the spectrum.

Advanced signal processing methodologies, encompassing techniques such as the Short-Time Fourier Transform, Continuous Wavelet Transform, and Hilbert-Huang Transform, have undergone assessment and demonstrated efficacy in specific research contexts. Nevertheless, their utilization introduces complexity and proves less applicable to extensive grid scanning. Consequently, our primary emphasis in this paper centers on the widely acknowledged approach involving Fourier amplitude spectrum analysis using the Fast Fourier Transform (FFT), as explained above.

Since the impact-echo method is based on resonance frequency measurements, it is highly sensitive to the dynamic behavior of the sensor unit, including the quality of the coupling between the impactor and the sensor as well as the stability of other contact regions between

the drone and the targeted structure. Both the sensor and the impactor need to be simultaneously in contact with the inspection target to ensure a successful data acquisition, this aspect is a significant challenge in the development of the robotized sensor unit. This also establishes a connection to the "Merkblatt B11" of the German Society for Non-Destructive Testing (DGZfP) [9], which provides guidelines for traditional impact-echo testing.

Mechanized and robotic inspection systems are increasingly used to improve the efficiency, precision, and repeatability of inspection processes [5,32]. Especially in areas that are dangerous or difficult to access, mechanized inspection systems are of high interest. In particular, recent technological advancements and the wide availability of uncrewed aerial vehicles (UAVs), also known as drones, make them interesting for inspection purposes in civil engineering. Aerial inspections are a key method of inspecting facilities with little to no standard method of access. They also reduce inspectors' health and safety risks and the possibility of human error. A recent study [23] compares robotized UAV inspection of bridges to conventional manual inspection carried out by humans and confirms the high potential of UAV inspections regarding time and reliability of results. In addition, the data acquired from the multiple embedded sensors and cameras, which are necessary for the stability and control of the UAV itself, often constitute a valuable source of information for the analysis of inspection results. Most commercially available systems so far are focusing on non-contact inspections, such as visual inspection or mapping [34]. In [10] various non-contact inspections techniques mounted on drones such as LiDAR, visual cameras, and infrared are comprehensively reviewed and presented. These achievements accelerate, in general, the development of multicopters and make the use of drones more user-friendly and commercially interesting. Lately, solutions have been developed that allow for contact inspection thanks to stability and control breakthroughs. The ability of a drone to apply forces to structures was shown in [1]. The respective authors presented a quadrotor platform that is able to apply a constant force of 5 N while maintaining its flight stability. Furthermore, this platform was already able to carry a payload of 200 g while having a flight time of six minutes. In [24] a general control model scheme for the interaction of UAVs with structures is presented, which covers different types of interactions between multiple UAVs and between UAVs and objects. The concept was demonstrated on autonomous helicopters, which were used for aerial manipulation tasks as well as load transportation. Additionally, [43] and [39] especially encourage the use of omniorientational flying platforms that have fixed tilted rotors, and thus, these systems are able to apply forces in all directions. In [30] a system of flying quadrotors is presented that can grab and transport objects. Furthermore, [27] presents a project where parts of the infrastructure are assembled using quadrotors. Within the framework of the AEROARMS project in 2018, ultrasonics and eddy current sensors were integrated into a multirotor drone with the goal of testing and inspecting metallic pipes [35]. Additionally, another UAV system was equipped with a single crystal ultrasonic gauge to perform wall thickness measurements of metal plates [16]. Another recent UAV development was targeting the analysis of powerlines by magnetic field strength measurements [47]. A flying corrosion inspection robot that uses the half-cell method to measure the potential field on steel-reinforced concrete was presented by [36] and is based on an omnidirectional drone platform [4] equipped with a special lightweight half-cell probe. This system was developed to inspect the rebars of steel-reinforced concrete structures.

When developing drone-based inspection systems, rotor-induced vibrations pose a significant challenge, often arising from sources such as propeller imbalance, aerodynamic loading, motor harmonics, and structural resonance. A review about different vibrations sources and control strategies has been presented by Candeloro et al. [6]. These vibrations can negatively impact camera stability and degrade sensor performance, leading to blurred imagery and inaccurate data collection. To address these issues, both active and passive damping systems have

been explored in past studies as effective mitigation strategies. Fu et al. proposed an optimized rubber material to reduce the negative effect of vibrations on UAV Lidar sensors [11]. And an active damping system to mitigate vibrations on drone cameras has been presented by [48]. Shin et al. proposed mode decoupling for vibration isolation on drone systems [42]. Additionally, real-time flight controller adjustments offer a dynamic approach to minimizing vibration effects during flight. For instance, Geronel et al. proposed an adaptive sliding mode control to reduce vibrations and their harmful impact on drone payloads [13]. Signal processing techniques such as filtering also play a crucial role by enhancing the quality of measurements despite the presence of residual vibrations. For instance, Li et al. combine different hardware damping components with low-pass filtering to improve on-board sensor accuracy in micro-UAVs [26]. In addition to the previously discussed sources of rotor-induced vibrations, additional vibrations can be introduced during physical contact with external surfaces. These contact-induced vibrations often result from dynamic interactions like bouncing or sudden impact forces at the point of contact. [15] discusses that effective mitigation may require a combination of mechanical damping and appropriate contact support structures, adaptive control strategies, and advanced signal processing to preserve system performance.

Whilst many automated aerial NDT systems have been developed for metal inspections, a gap remains in the development of similar systems for concrete structures. NDT for concrete structures differs from NDT methods used for metals due to the distinct material properties and expected failure mechanisms. While drone-based NDT systems have been developed for metals, they cannot be directly applied to concrete structures without modification. For example, the significant variation in acoustic damping properties between concrete and metal necessitates the use of different operating frequencies for elastic wave-based inspections. Metals typically require frequencies in the range of hundreds of kilohertz, whereas concrete inspections are conducted at frequencies below 100 kilohertz. This disparity influences the design of probes used for each material. Furthermore, ultrasonic testing of metals generally requires a coupling agent, such as water or ultrasonic gel, to facilitate wave transmission, while acoustic inspections of concrete can be performed using dry-contact probes. Instead, effective drone-based NDT for concrete must be developed by adapting material specific structural diagnostic techniques, such as impact echo or ultrasonic testing with DPC (dry point contact) probes, to ensure accurate assessment and reliable inspection capabilities. In particular, systems that can surpass the limitation of visual inspection and are capable of characterizing embedded flaws whilst also measuring concrete's mechanical properties (e.g., strength). The current paper aims to reduce this gap. Earlier works by the authors discussed the general need for automated concrete inspection systems and introduced the conceptual idea of the technology presented here [33,44]. The current work provides in-depth reports on the execution of the original concept and is divided into five sections: (1) the description of the design of the sensor including mechanical, electrical, and software aspects; (2) the details of the testing and experimental set-up of the in-laboratory flight tests; (3) the signal processing and post-processing methods applied are described, including specific filtering as well as volumetric imaging techniques employed; (4) the results of the flight tests are described; and (5) the paper concludes with a discussion of the results and an outlook on future works.

This research presented herein is centered on the utilization of contact-based impact-echo techniques for NDT. This paper presents a novel drone-based impact-echo inspection system for the structural health assessment of concrete structures. A drone-based impact echo inspection system significantly improves accessibility, particularly for bridge inspections and high-rise buildings, by reducing inspection time and enhancing safety without the need for scaffolding; however, a challenge is the weight constraint, which – in comparison to traditional impact-echo inspections - necessitates the lightweight design of sensor units. The primary objective is to address the inherent challenges associated with the integration of a contact-based acoustic methodology

onto a UAV (drone), thereby facilitating the deployment of drone-based impact-echo assessments. This research distinguishes itself from conventional drone inspections, primarily reliant on visual assessments. Furthermore, it deviates from the domain of SHM applications, which rely on permanently affixed sensors. Consequently, this paper concentrates on the direct implementation of NDT methodologies, specifically impact-echo, for acquiring localized and specialized information while the drone is in flight.

2. Materials and methods

2.1. UAV robotic platform

The UAV inspection system used consists of the *Voliro T* flying robotic drone [20,49] and the novel sensor unit developed for this research. It is a unique platform suitable for contact-based inspection techniques. The flight controller has been developed by Kamel [19] with the specific purpose of enabling physical interaction between the drone and different structures. Fig. 1 shows the developed sensor unit mounted on the drone. The sensor unit is connected to the drone platform through a bayonet and is rapidly interchangeable. The payload-to-drone interface is designed such that it can supply 5 V and 12 V as well as transfer data through a USB or Ethernet protocol. The drone is complemented with two remote controllers; one is dedicated to the pilot and contains two first-person view (FPV) cameras, and the second is dedicated to the inspector and displays the collected time signals in real-time during the inspection. Each collected signal is finally stored together with the respective photo from the camera, which can be used in post-processing and reporting. The flight time with one battery is approximately 16 min and the batteries can be easily and quickly changed during the inspection job through a click closure. The position of the drone is controlled through GPS (in case of outdoor inspections) or optical flow sensors (in case of indoor inspections). The reading of the positioning accuracy of the measurement location can be further improved by equipping the drone with a laser reflector prisma and connecting it to a laser ground station. As of now, the flight controller of the drone has a manual pilot mode; however, automated flight modes along pre-defined flight paths, for instance, for automated grid collections, could be imagined to be implemented in the future.

The drone platform is capable of applying a constant contact force of around 20 N for up to 5 s while maintaining its stability. During this contact mode the drone platform can withstand winds of up to 8 m/s. It can continuously pitch within a range of 180°, leading to great flexibility in the surface's angle (or wall orientation) it can inspect; some examples are shown in Fig. 2. The figure shows the drone inspecting (a) a concrete block on the ground, (b) a concrete wall, and (c) a concrete ceiling, respectively. Those two features, i.e., the in-flight contact and the orientation flexibility, are crucial for contact inspection applications.

The drone is able to carry a payload, namely the sensor unit, of up to 800 g to 1100 g, depending on the center of gravity and inertia behavior



Fig. 1. Inspection drone with novel impact-echo sensor unit mounted.

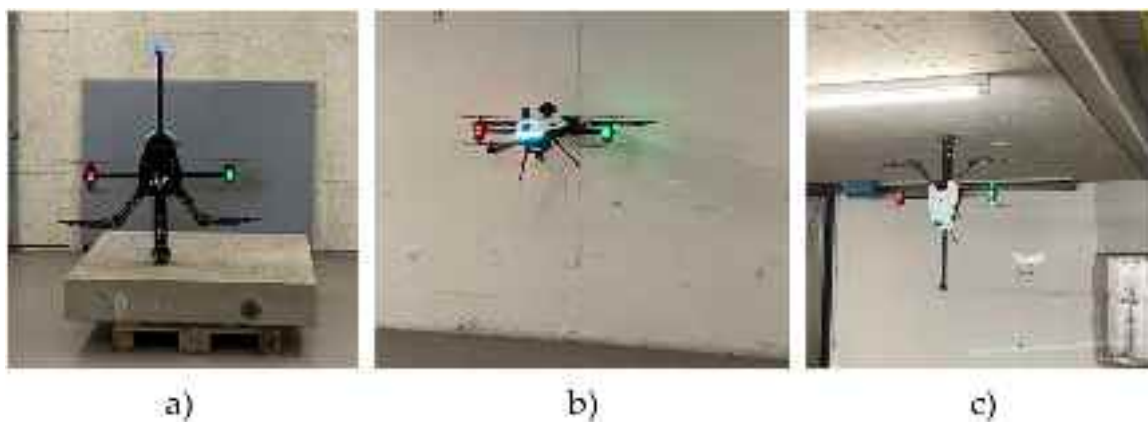


Fig. 2. Drone during operation applying mechanical contact force to component surfaces in different operations: (a) measuring on the ground, (b) measuring on a vertical wall, and (c) measuring at the ceiling.

of the payload. This weight restriction is one of the main challenges to the development of a sensor unit for concrete inspections. A typical hand-held measurement device weighs around 2.5 kg. Furthermore, the size and geometry of the sensor unit have to be designed in a way that does not obstruct the FPV cameras nor the optical flow sensors. Additionally, the sensor unit development requires full mechanical, electronic, and software integration and communication between the interfaces. The application of the impact-echo method requires stable and reliable sensor- and impactor-to-surface coupling conditions for each measurement.

While drone-based inspections provide a high potential to overcome limited accessibility (i.e., high buildings) and thus also increase the safety for inspection personnel (no need to expose personnel to risky working conditions at height), there are specific safety issues that need to be addressed during drone inspections. Apart from the need to check flight regulations prior to inspection, the area has to be secured with “flight zone” signs. Furthermore, it has to be ensured that the pilot and inspector are in a safe location at least 5 m away from the inspection and take-off area. The pilot has to ensure visual contact to the drone system at all times. In case of a malfunction of the drone the drone has an emergency mode that cuts off power instantly through a switch at the remote controller. This will force the drone to crash but prevents it from crashing into people. Safe operations require standard personal protective equipment such as helmet, goggles, gloves, and ear protection. As of now, the drone is manually piloted and does not have obstacle avoidance or autonomous flight control; these capabilities are not the focus of the current study but could be considered in future research to further increase safe operation of the drone system.

2.2. Sensor unit design

During the project, an impact-echo sensor unit was designed for the drone platform. This unit contains an automated impactor and a sensor, both commercially available from *Olson Instruments*. Since the drone platform is able to apply contact forces which allows to use contact-based NDT, the current development focuses on contact impact-echo. This sensor and impactor choice was motivated by the fact that both have been widely tested in previous studies, are widely used and accepted in industry, and are considered reliable for standard manual impact-echo measurements [45,46]. Furthermore, this system provides meaningful inspection results using a single sensor weighing 520 g, rather than requiring an array of sensors, thereby making it less challenging to meet the weight constraints of the drone. Alternatives such as DPC-based ultrasonic testing for concrete generally offer more advanced imaging solution than impact-echo only when a high number of probes are used. However, these advanced solutions typically weigh several kilograms and have high energy consumption, making them less suitable

for drone-based applications as they would exceed the payload weight limit of 1.0 kg. As a result, a single-sensor impact-echo configuration was chosen to meet operational requirements while staying within acceptable weight constraints. This approach ensured functionality while minimizing the impact on the system's mobility and stability. The impactor used in this study is an automated solenoid mechanism based on an electrically powered coil. It is securely fixed within the sensor holder to ensure that the distance between the impact and the probe remain the same for all measurements and both share the same positioning accuracy, improving measurement consistency. The impactor features a cylindrical tip with a diameter of 5 mm and delivers an impact energy ranging from 0.011 to 0.019 joules at a typical operating current of 5 amps. To initiate an impact, a signal is sent from the remote controller to the drone's onboard computer, which then triggers the solenoid. This process enables precise and repeatable excitation of elastic waves for impact-echo testing.

The sensor and impactor were fully integrated into the sensor's arm, considering mechanical, electrical, and software integration. Changes were applied to the original impact-echo device to adapt it to the requirements for the remote operation of the sensor unit. The push button used for the impactor actuation was replaced by an electrical input from the drone, which can be triggered using the drone's remote control. The batteries were removed and replaced with a power line sourcing the power directly from the drone. The original external casing was removed to rearrange the positioning probe, sound card, and impactor in the newly designed unit. Ground tests were performed after implementing the changes to ensure the functional integrity and the sensing performance of the device was unaltered. These tests are further discussed in the next sections.

The new sensor unit consists of an electrical hardware and software interface to the drone platform, an electrical unit, a mechanical support structure and sensor holder, a USB soundcard to digitalize the signal, a software code to read the sensor data, and a payload cover that protects the sensor components from environmental influences such as dust. The entire sensor unit weighs around 900 g. The collected signal is a time domain waveform that is later converted into the frequency domain through FFT.

The sensor unit and the drone are connected through a payload interface where both electrical pulses, as well as USB signals, can be transmitted. The sensor, sensor board, and sound card are continuously powered. The data recording of the signal is timely adjusted to the impactor. The impactor itself is activated through a separate port by sending an electrical pulse signal that is triggered by the pilot from the remote controller. The signals themselves are collected through the onboard drone computer. During data collection, the raw signal is stored on an SD card and displayed on the inspection tablet in real-time. This allows the inspector to make a real-time decision on the signal

quality. The inspection tablet with a live signal enables real-time assessment of coupling, as poor coupling results in a signal containing only noise, allowing for immediate corrective action and retaking the measurement in case of minor distractions, such as small pitch offsets. After the data collection the data is transferred to a computer and further processed in a volumetric manner (see Section 2.4). While data collection is fast and not very resource-intensive, the detailed signal processing requires in-depth analysis by a knowledgeable expert and is currently not easily automated. Therefore, the detailed signal processing and data analysis is performed afterwards on a laptop. Both remote controllers are shown in Fig. 3.

The assembled sensor unit is shown in Fig. 4. It consists of the sensor unit head and a sensor unit arm. The sensor unit head carries the sensor as well as the impactor through a sensor holder. The sensor unit arm houses the electronics, the sound card, and the payload interface. It also has an embedded status LED visible for the pilot during flight through the onboard camera that informs about the health status of the sensor before data acquisition.

The design of the sensor holder was a crucial part of the entire design as its stiffness behavior influences the dynamic response of the unit and is subjected to trade-offs. On the one hand, the sensor holder must have enough stiffness to carry the high weight of the sensor of around 520 g, and on the other hand, it must be sufficiently compliant to be uninfluenced by small movements of the drone's main body (i.e., due to gusts). The ability of the sensor unit to tilt in order to maintain stable coupling conditions with a surface, for instance, in the event of gusts, is illustrated in Fig. 5.

The sensor holder design as well as the 3D printed part are shown in Fig. 6. The four spring-type compliance elements are designed to be stiff enough to carry the sensor. The sensor itself is placed in the middle of the sensor holder head to ensure good coupling conditions of the sensor and the inspected surface. The impactor is placed below the sensor to ensure that the drone's optical flow sensors and camera views are not obstructed. The six feet of the sensor holder were manually adjusted to compensate for initial tolerances and to ensure the sensor and the impactor were kept at an appropriate distance from the wall. The feet' length was adjusted during ground testing (manual manipulation of the



Fig. 4. Picture of the assembled sensor unit.

drone and sensor unit) on the concrete test block. The sensor holder is 3D printed by an HP Multi Jet Fusion 3D printer (MJF) and is made from polyamide.

The software section that reads the sensor data was programmed in C++, uses the portaudio library [37] and reads the audio signal digitized by the USB sound card in the time domain. The signal length can be up to 90 ms and its sampling frequency is 44.1 kHz. The signal is stored in a float point precision binary format.

Experience has shown that wind speed has no impact on the impact echo measurement as long as it remains within the specified limits of the drone systems. Similarly, temperature and humidity has not affected the measurement's accuracy so far. However, flights cannot be conducted in the presence of visible moisture and temperatures below 10 °C (risk of icing on the blades) or heavy rain, as it may compromise system performance.

The drone-based impact-echo system is designed for both indoor and outdoor use, with a recommended maximum wind speed of 6 m/s to ensure precise interaction with the surface. To achieve accurate results, the acquired signals should be checked for quality. If poor coupling is detected, the pilot should first attempt to retake the signal in the same contact mode. If the signal does not improve, the drone should be detached from the wall and the contact should be re-established at the



Fig. 3. Drone remote controllers, left: pilot remote controller and right: inspector remote controller.

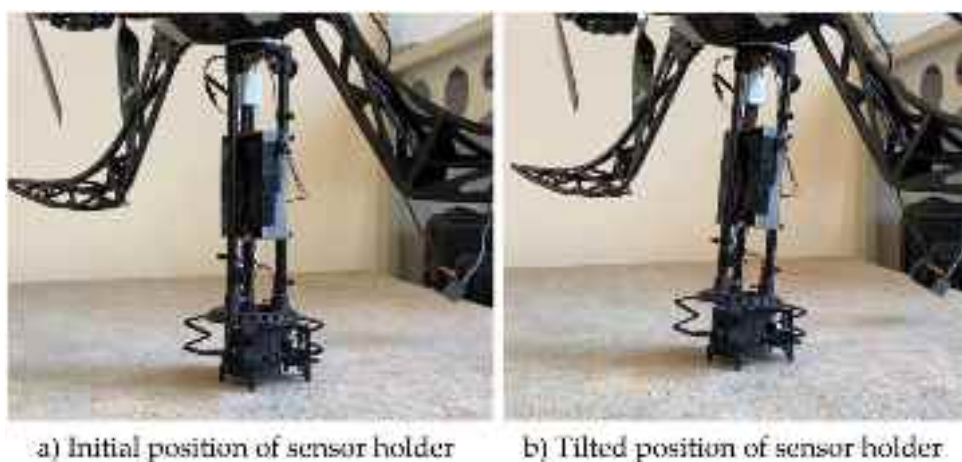


Fig. 5. Illustration of the sensor's holder resilience to gusts and ability to maintain stable contact conditions.

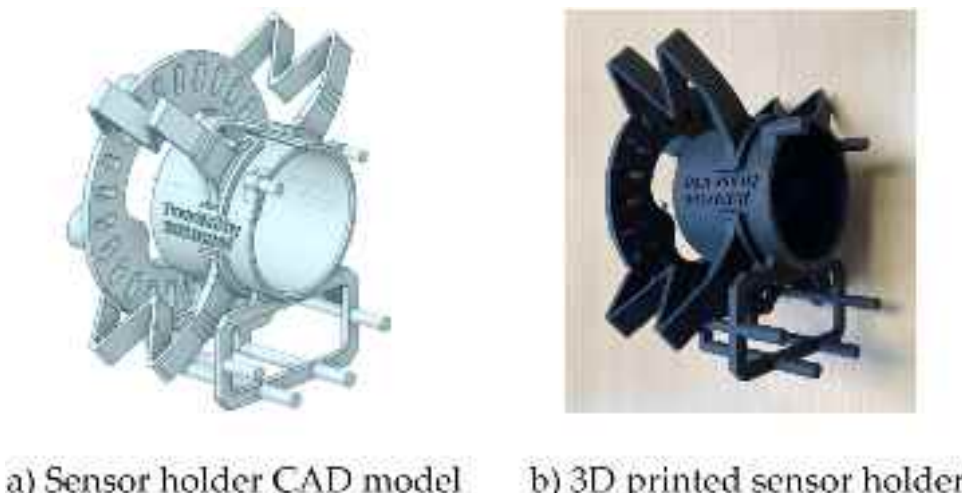


Fig. 6. Sensor holder design.

same location. If the issue persists, the pilot should reposition slightly and re-establish the contact at a nearby location to achieve better coupling. A summary of the system's technical specifications can be found in [Table 1](#).

2.3. Testing and experimental set-up

The tests conducted as part of this research can be divided into three types:

- Test 1: ground testing with horizontal measurements,
- Test 2: flight testing with horizontal measurements,
- Test 3: flight testing with vertical measurements.

The purpose of the ground testing was to evaluate variation in the sensing quality of the impact-echo system during the development phase of the sensor unit (or payload), independently from the influences of flight conditions on the impact-echo data. During the ground testing, the sensor unit was manually held and positioned at defined measurement locations on the concrete test block. The flight testing was conducted once the sensor unit was fully integrated into the drone and the drone was flying. It must be noted that during the first ground test, a reference measurements series was obtained and used to build a reference impact-echo image of the original impact-echo device before its integration into the payload. This reference measurement series was used as a

comparative baseline to assess the quality of later measurements and refers to the result of Test 1 in this paper. Subsequent ground tests were conducted iteratively during the integration phase for fine-tuning the sensor holder's design. These iterative tests are not discussed in this paper since they have limited relevance beyond the development phase.

Test 1 and Test 2 were conducted on the same reference concrete block shown in [Fig. 6](#), which was originally designed by BAM (*Bundesanstalt für Materialforschung und -prüfung*) in Germany for training purposes. This block design is also referred to as "Radarplatte" (radar slab) and contains features detectable with traditional impact-echo inspection devices. These features include an artificial delamination defect (simulated with an embedded piece of Styrofoam) and a tendon duct crossing the block lengthwise and partially grouted (halfway), both are shown in [Fig. 7](#) and further described in [Table 2](#). The detection and accurate positioning of these two features by the drone and impact-echo payload served as the main criteria for assessing the success and effectiveness of this new inspection method and as validation of Test 1 and Test 2. The typical way of conducting impact-echo measurements is by collecting data in a grid pattern. The measurement's grid density varies on a case-by-case basis depending on the desired accuracy and the time restrictions but is often set within a range of 50 mm to 200 mm. Once the measurements have been collected, the data is usually analyzed in the frequency domain, and the inspection analyst looks for changes in the frequencies displaying the highest amplitudes in the frequency spectrum. In the case of Test 1 (ground testing) and Test 2 (flight testing)

Table 1

Summary of the system's technical specifications.

Technical specifications of the system	
Drone platform	Voliro T research platform
Cameras	2 FPV cameras, 1x normal angle, 1x wide angle
Flight time	16 min
Flight mode	Manual piloting, stabilization through GPS or optical flow sensors
Wind limits for interaction	8 m/s
System temperature limits	-10 °C to 40 °C
Additional weather requirements	flights cannot be conducted in the presence of visible moisture and temperatures below 10°C or heavy rain
Pitch	-90° to + 90°
Contact mode	20 N, 5s-10s
NDT Technique	Contact-based Impact-Echo
Sensor	Olson Instruments
Impactor	Olson Instruments automated solenoid, impact energy ranging from 0.011 to 0.019 joules
Sampling Rate	44.1 kHz
Post-Processing Software	echolyst
Data acquisition	Through drone computer
Triggering of impactor	Through drone remote controller
Sensor-unit weight	~900 g
Max. supported payload weight	~ 1000 g
Remote controllers	1x pilot tablet, 1x inspector tablet
Assembly time	< 5 min

with horizontal measurements), a total of 121 measurements were collected in a grid pattern centered on the concrete block as shown in Fig. 7a and described in Table 2. A 100 mm spacing was maintained between the measurement points in the grid. Since the grid was centered on the block, the shortest distance from any measurement point to the block's edge was 100 mm. The maximum deviation error caused by inaccuracy in the drone positioning was estimated to be 20 % (20 mm).

The purpose of Test 3 was to demonstrate the drone's ability to perform impact-echo measurements in orientations beyond the horizontal plane measured in Test 1 and Test 2. Unlike previous experiments conducted on the same concrete reference block, Test 3 was carried out on a vertical wall shown in Fig. 8. The decision to use a wall, rather than the reference block, was necessitated by the latter's substantial weight and size, which precluded reorientation due to health and safety concerns. Consequently, the results of Test 3 are limited to a thickness assessment based on four impact-echo measurements collected along a horizontal line, rather than a grid acquisition with validation against a known reference. The wall thickness was determined with 8 manual impact-echo spot measurements at different locations on the concrete wall and showed a mean value of 24.1 cm with a standard deviation of

0.2 cm using a sound velocity of 4030 m/s for evaluation of the thickness. This value was used as a reference for validating the impact-echo thickness assessment in Test 3. This test provides a preliminary insight into the system's performance when applied to in-situ conditions and different pitch angles than shown in Test 1 and Test 2. Besides showcasing the system adaptability to different surface conditions and pitch angles, Test 3 also underlines the system's feasibility in obtaining meaningful thickness profiles and impact-echo data even with a limited set of measurements.

The tests presented in this study were designed to assess the feasibility of impact-echo inspection using a drone. In addition, they provide an insight into the system's adaptability and accuracy as well as an outlook on how this approach can be implemented in future large-scale in-situ inspections and in different applications. The scope of these tests was limited to vertical and horizontal measurements. Nevertheless, owing to the drone's ability to exert controlled and stable contact forces in any orientation, the measurements obtained in this study (i.e., Test 2 and Test 3) are considered representative of the expected performance of this drone-based inspection system across different orientations.

2.4. Signal processing and volumetric imaging

The collected results from both, the reference testing and flight testing, were analyzed in a volumetric visualization. Fig. 9 summarizes the signal processing workflow applied to the impact-echo data and their interpretation into mapped dataset. This level of analysis was achieved using the internally developed and commercially available inspection PC software *echolyst* [2]. Whilst the manual reference test was acquired and processed using *echolyst* (through a cable connection), this was not possible with the cable-free data transfer of the drone. Instead, in the case of the flight test data, an additional software interface was developed to handle the cable-free data acquisition and convert the raw time signal into *echolyst* input data that can be handled into a 2D or 3D

Table 2

Description of the measurement grid and concrete block specifications used in test 1 (ground testing) and test 2 (flight testing with horizontal measurements).

Measurement grid specifications	
Total number of measurement points	121
Measurement grid size	1100 mm × 1100 mm
Distance between measurements	100 mm
Concrete block features' specifications	
Block dimensions	1200 mm × 1200 mm × 200 mm
Delamination dimensions	600 mm x 300 mm
Delamination depth	150 mm
Tendon duct depth	80 mm

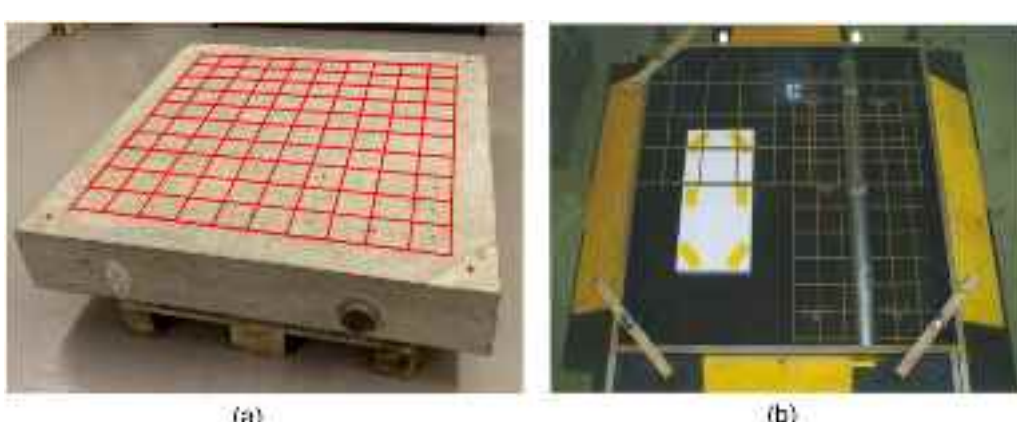


Fig. 7. (a) Illustration of the measurement grid pattern used for acquiring data on the concrete block, (b) Picture of the concrete block mold and features - including artificial delamination with Styrofoam and metal tendon duct – before the cement mix was poured.



Fig. 8. Left: picture of the wall, and right: measurement location used in test 3 (flight test with vertical measurement).

representation of the gridded dataset. The original signals obtained with the drone are 90 ms long. This interface crops each original signal into a section of interest spanning over 15 ms and containing the impact-echo signal. As an initial step, the original signal is filtered using a high-pass filter. The cut-off frequency can be manually adjusted by the inspector and is usually set around 1.5 kHz. This also ensures that the rotor-induced vibrations are filtered out which are below 100 Hz in the current experimental set-up. In the next step, the onset of the impact-echo signal was identified by looking for an amplitude rise above an arbitrarily set threshold in order to distinguish the signal of interest from the noise. The threshold value was selected based on multiple laboratory experiences and observation of the expected amplitude response from the concrete structure. An example of such amplitude response is illustrated in Fig. 10, which shows a standard raw signal collected during flight testing and containing an impact-echo response with an onset at around 35 ms.

The filtered and cropped signal is then transformed to the frequency domain using a Fast Fourier Transform (FFT). A key advantage of conducting impact-echo signal analysis in the frequency domain is its ability to mitigate the influence of noise on data interpretation, even when the signal-to-noise ratio appears low in the time domain. For noise to significantly disrupt impact-echo data acquisition, it must meet two criteria: it must exhibit sufficient periodicity to surpass the impact-echo signal in energy within the frequency domain, and its dominant frequency must fall within the unfiltered frequency range. The signal to noise ratio (SNR) was determined for each cropped and filtered signal (as shown in Fig. 10c), following Eq. 2 [12].

$$\text{SNR} = 10\log_{10} \frac{\text{RMS}_{\text{signal}}}{\text{RMS}_{\text{noise}}} , \quad (2)$$

The root mean square (RMS) value of the noise ($\text{RMS}_{\text{noise}}$) was computed using the first 30 samples of the signal. At this stage, the probe was already in contact with the structure; however, the impact-echo signal had not yet reached the probe. The root mean square value of the signal ($\text{RMS}_{\text{signal}}$) was determined using 30 samples taken at the onset of the signal response. This onset coincided with the arrival of the highest peak in the signal, typically observed at 2.3 ms, corresponding to the propagation of the surface wave from the impact location to the probe. The median SNR was found to be 10 dB, the mean was 8 dB and the standard deviation 7 dB. Amongst the measurements, 24 had a negative SNR value (20 % of the dataset), however most did not correlate with artifact in the resulting thickness profile (shown in Fig. 13) nor prevent the feature detection (shown in Fig. 15 and Fig. 16).

Following the conversion of the measured signal from time to frequency domain, they are ready to be visually analyzed and the frequency response to be interpreted into specific geometric features of the material. Hereby, it should be kept in mind that the frequency and depth coordinates are inversely proportional according to Eq. (1). The same wave velocity, c_L in Eq. (1), was used for all datasets and was set to

4030 m.s⁻¹. This velocity was calibrated based on the expectation that back wall thickness should be visible at a depth of 200 mm. Furthermore, the signals are indexed with a column and row index to map them to the pre-defined grid representative of the measurement area. A common analysis consists of isolating the dominant frequency component (i.e., the frequency with the highest amplitude response in the FFT) of each signal and plotting them in a contour plot representative of the measurement area (examples are visible in Fig. 12 and Fig. 13 of the results section). Additionally, the interpretability of impact-echo signals can be significantly increased by volumetric analysis and imaging. The frequency signals can be analyzed in more detail by looking at B-, C-Scan, and D-Scans where y-, depth- or frequency-, and x- values are kept constant, respectively. Thus, the resulting cross-sectional views can be evaluated along each grid line and contain all the signals collected along one line. The top views (XY-views) allow slicing the results. By plotting the signals as colored contour plots, they become much more intuitive for interpretation in comparison to single signals. This imaging strategy applied to grid scans leads to an entire X-Y-Z data 3D representation. Fig. 11 shows an illustration of these planes typically used for volumetric analysis of impact-echo measurements, namely for B-, C-, and D-Scans.

3. Results

3.1. Reference ground test

This section shows the results of the reference ground testing, also referred as Test 1 (as introduced in Section 2.3), obtained using the *echolyst* software. Fig. 12a) shows a thickness profile obtained from the reference dataset. This thickness profile provides an overview of the dominant frequency component found in the individual spectrum of each of the impact-echo signals from a gridded dataset.

Fig. 12b) shows a cross-section (B-scan projection) of the block, at a distance of 600 mm along the y-axis. This cross-section is strategically positioned to cross both the delamination and the tendon duct perpendicularly. Note that the bandpass filter setting of the software was left on its default settings (respectively 5 kHz high-pass and 18 kHz lowpass cut-off frequencies) for the data processing and visualization.

The main features of the test block are observable in the frequency response: the orange blob on the left side and the blue line on the right side of each image are consistent with the shape and position of the delamination and the tendon duct. The dominant frequency found around the delamination area is 13 kHz which corresponds to the expected depth of 150 mm (based on Eq. 1 and the set wave velocity of 4030 m.s⁻¹). Similarly, most of the background representing the back wall has a frequency of 10 kHz, corresponding to the block's thickness of 200 mm. The main frequency of the tendon duct is 7 kHz, which corresponds to a depth of 276 mm, hence placing the duct deeper than the back wall; however, Eq. (1) (which is based on the Lamb waves' behavior) does not apply to shallow objects. Instead, in shallow regions

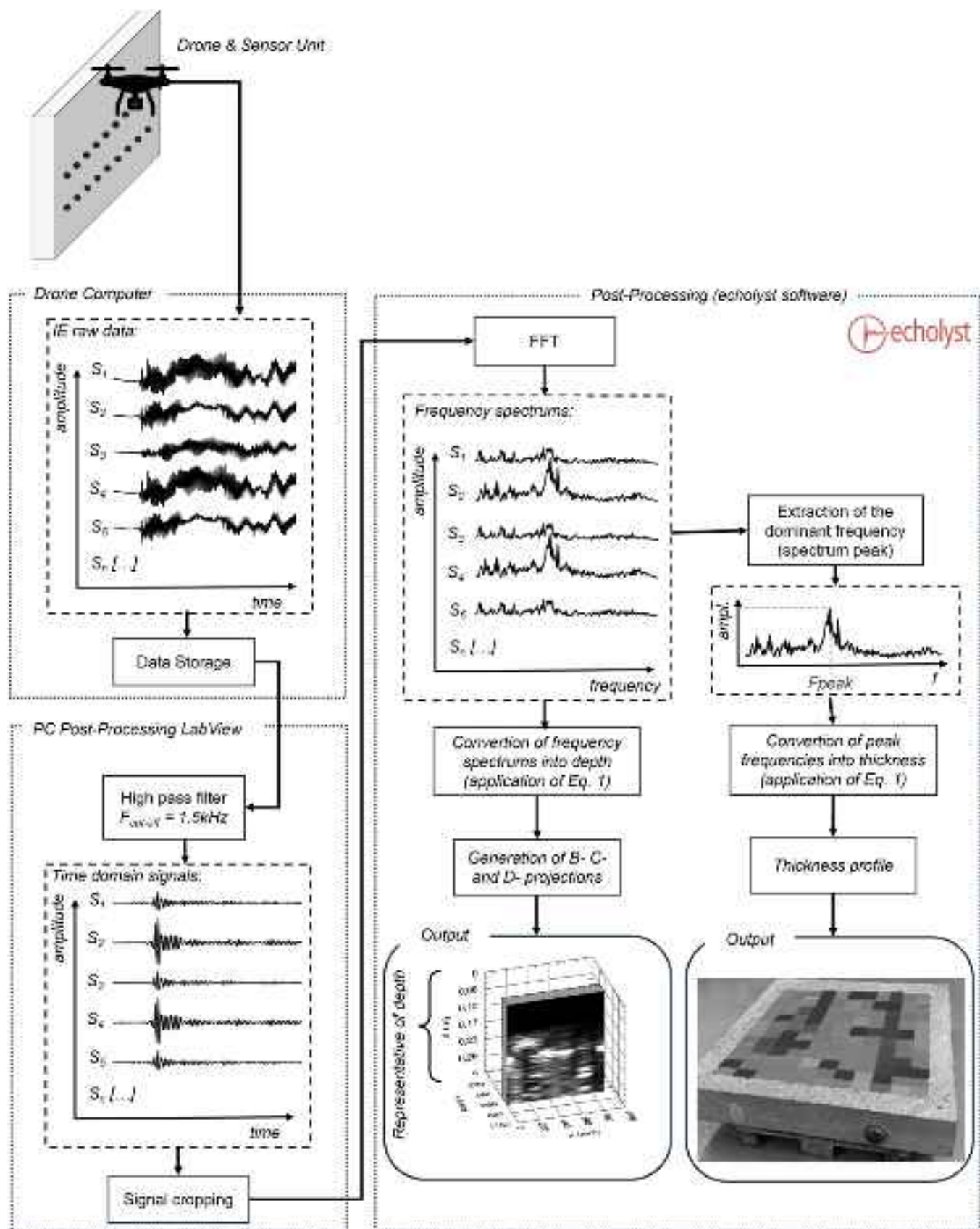


Fig. 9. Illustration of the data processing workflow applied to the impact-echo signal from the data acquisition to the mapping and visualization of the results in a format suitable for structural assessment.

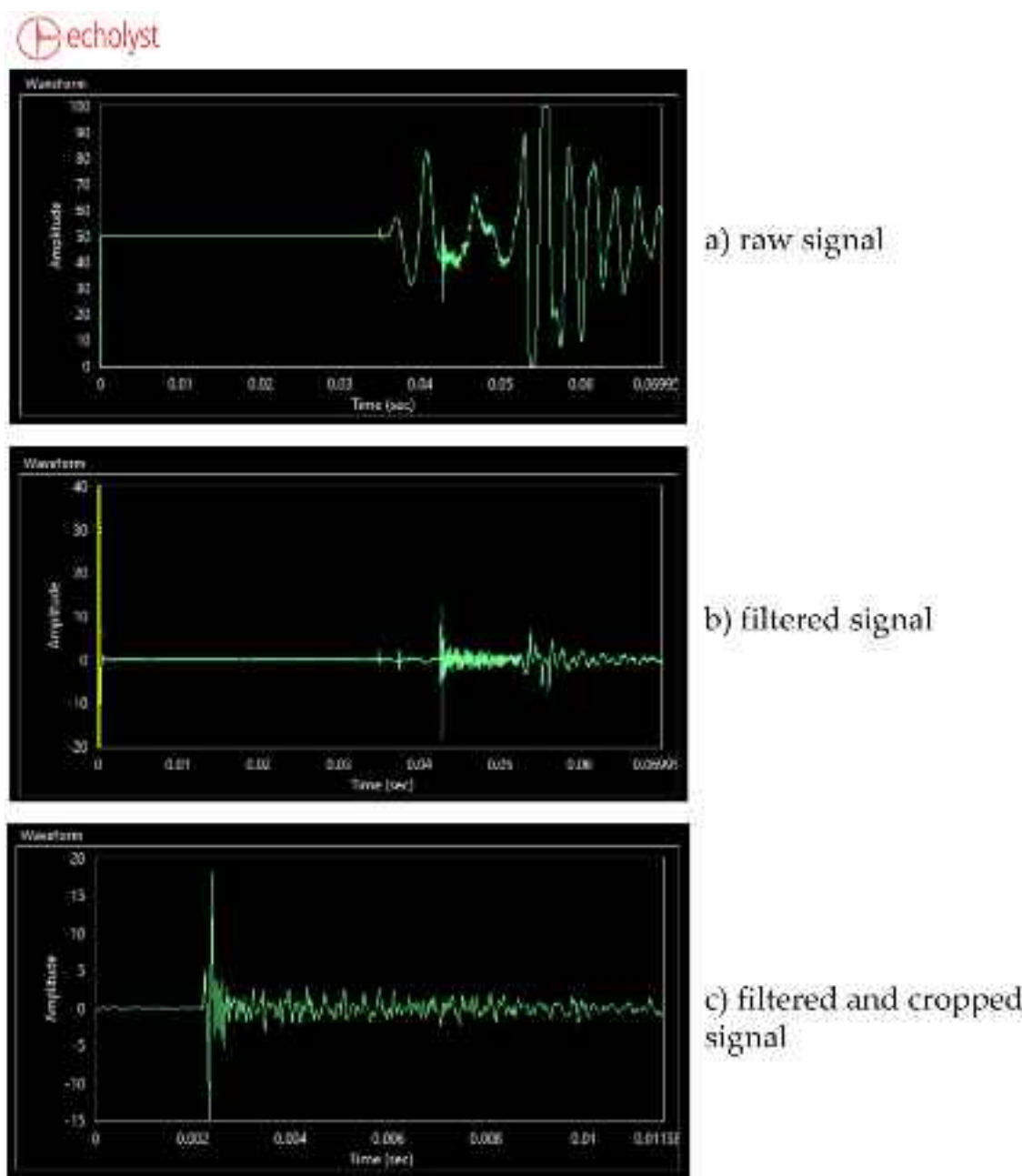


Fig. 10. Example time domain waveform collected with the drone and signal filtering and cropping before analysis: (a) raw signal, (b) filtered signal, and (c) filtered and cropped signal.

(approximately less than 100 mm deep) the flexural vibration mode dominates the spectral response, with maxima occurring at lower frequencies than with Lamb waves modes [22]. Although this phenomenon is preventing the localization of the duct's depth (which is known to be 80 mm) it does not affect the detectability of the duct and its positioning in the thickness profile of the block shown in Fig. 12a). This effect of the frequency's responses on the perceived depth positioning of the different geometric features is better depicted in Fig. 12b).

3.2. Flight test results grid measurements

This section shows the results of the flight test with horizontal measurement on the reference block, which are referred as Test 2 in Section 2.3

The maximum frequency peaks of the spectrum were analyzed for each measurement point in the grid, leading to a 2D image representing

the block frequency response. Fig. 13 shows the respective results overlaid with the concrete test block. The color scheme represents the thickness calculated from the maximum frequency peaks according to Eq. (1). The back wall of the concrete block itself appears at 10 kHz and is represented with a bright green color, which corresponds to 20 cm. The resulting image shows features indicating the presence of the tendon duct, which appears at around 7 kHz (corresponding to a depth of 276 mm) as well as the delamination, which appears at around 13 kHz (corresponding to a depth of 150 mm). The frequency responses of the different geometric features delamination, tendon duct, and back wall are consistent with the previous observation from the analysis of the reference ground test dataset in Fig. 12.

Fig. 14 presents the histogram of the observed thickness indications derived from the dominant frequency indication. The left plot considers the entire scan area, while the right plot focuses exclusively on the section of the scan grid that covers the delamination region. Taking into



Fig. 11. Definition of B-, C-, and D-Scans illustrated on the concrete test block. Note that in the axis direction f or d may be represented as frequency (f) or thickness (d) in the scans.

account the entire grid gives a mean value of a thickness of 20.1 cm and a standard deviation of 5.8 cm. For the delaminated section specifically, a standard deviation of 7.0 cm is obtained. This corresponds with a diffuse indication of the delaminated section.

Two B-Scans and one C-Scan are evaluated, each highlighting elements of interest in the block. The B-Scan at $y = 600$ mm represents a cut in the middle of the block where the delamination and the tendon ducts are present. The B-Scan at $y = 200$ mm represents a cut through the block away from the delamination where only the tendon duct is present. The C-Scan represents a position where the tendon duct is expected to be visible.

Fig. 15 shows the B-Scan of the measurements at the test block in the middle of the test block ($y = 600$ mm). The color scheme represents the signal amplitude in a normalized arbitrary unit. At a depth of 200 mm, the back wall is visible at the expected location. Furthermore, both the delamination as well as the tendon duct are visible in the B-Scan at their expected frequency according to Eq. (1). Again, the results of the flight test in **Fig. 15** are similar to their equivalent reference ground test results previously shown in **Fig. 12b**.

The similarities found between the flight test and ground test results, both in the thickness profile (**Fig. 12a**) and **Fig. 13** and the B-projections (**Fig. 12b**) and **Fig. 15**), confirm that the sensing capabilities of the impact-echo system are retained following its integration on the drone and under flying conditions.

A B-Scan representing the impact-echo measurements collected

closer to the edge of the concrete test block ($y = 200$ mm) is shown in **Fig. 16**. The B-Scan shows the back wall as well as the tendon duct. As expected, the delamination is not visible anymore at this location. With this strategy of analyzing the B-Scan subsequently at different locations the size and specifically the x- and y-extension of the delamination can be determined which is particularly important for diagnostics and assessments of built infrastructure and to achieve a good data basis for repair decisions.

Fig. 17 shows the C-Scan of the results at around 7 kHz. The color scheme represents the signal amplitude in a normalized arbitrary unit. From the C-Scan the top view of the tendon duct can be identified. In combination with the B-Scans shown before, this allows a robust localization of the tendon duct in x- and y-direction within the concrete block. The C-Scan shows two interruptions of the tendon duct, which means that these measurement points are not absolutely accurate. It is assumed that this is due to non-optimal coupling, which indicates the coupling needs to be further optimized in order to obtain robust results at every measurement point. Thus, for field testing, we suggest increasing the grid density to account for a potential data dropout of up to 15 %. But overall, it can be said that the tendon duct is still clearly visible with the current inspection system.

clearly visible with the current inspection system.

The following **Table 3** compares and summarizes the results from the ground and flight tests on the concrete test block. The metrics that are

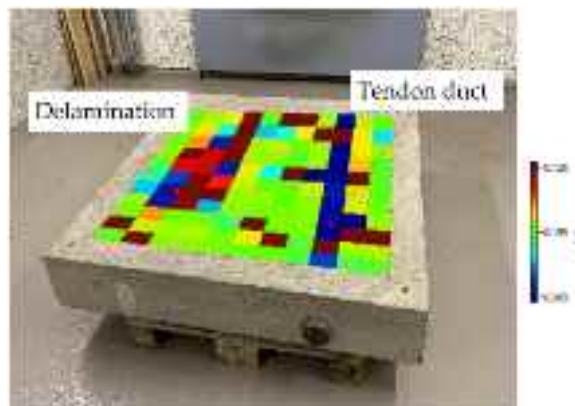


Fig. 13. Overlay of test block with the maximum frequency peaks from the horizontal flight testing dataset (thickness profile).

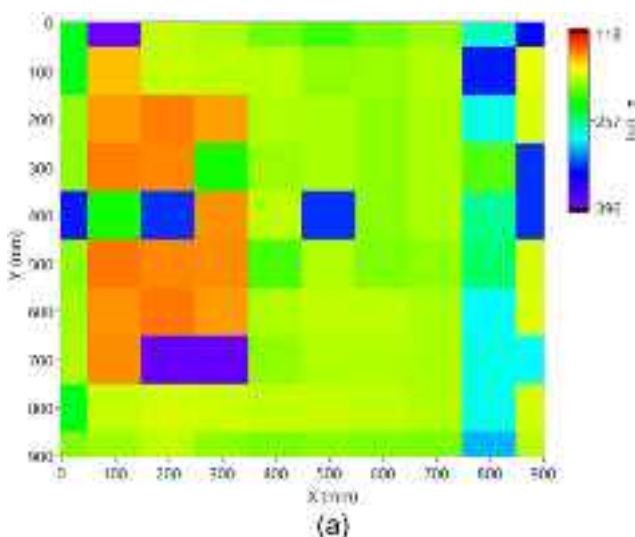


Fig. 12. Results of the reference ground testing dataset.

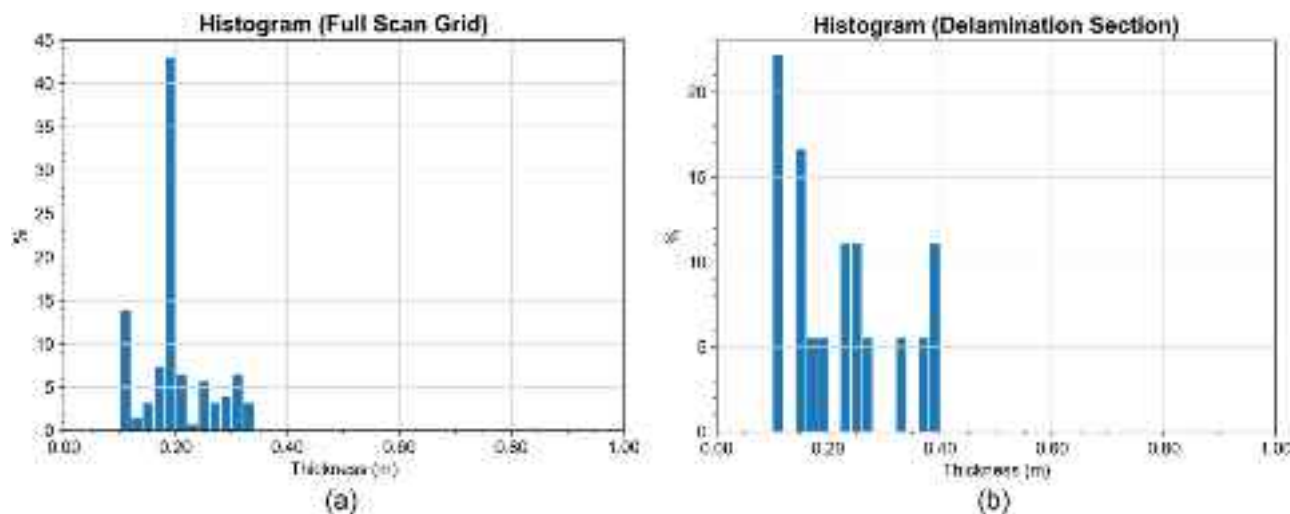


Fig. 14. Histogram of thickness derived from the dominant frequency. Left: taking into account the entire scan area. Right: delamination section.

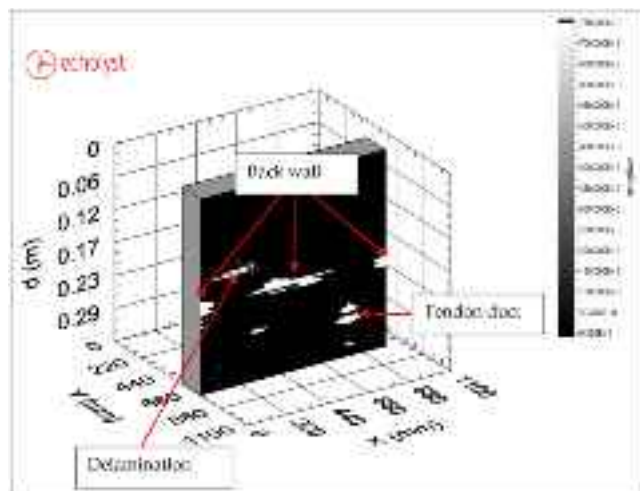


Fig. 15. B-Scan of the test block, visualizing the tendon duct and the delamination at $y = 600$ mm obtained from the flight testing dataset.

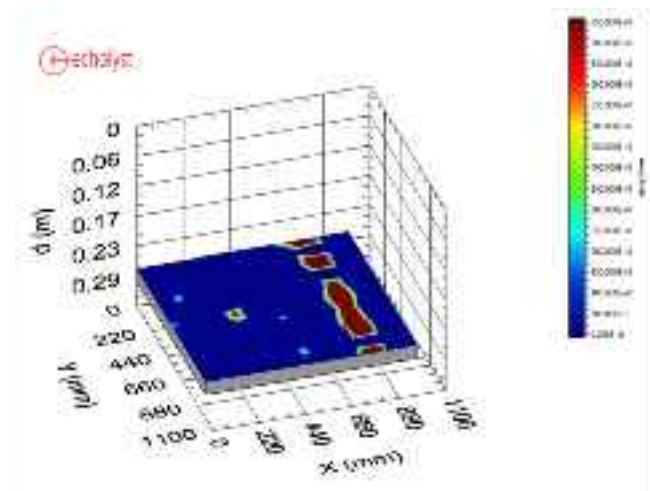


Fig. 17. C-Scan of test block visualizing the tendon duct.

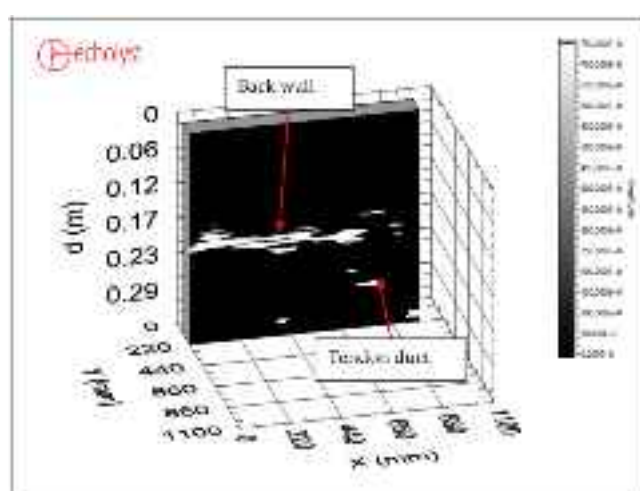


Fig. 16. B-Scan of the measurements at the test block visualizing the tendon duct at $y = 200$ mm.

evaluated for comparison are the mode referring to the maximum peak in the histogram, the median value as well as the 25 % and 75 % percentile of the histogram. These metrics were chosen, because the values in the histogram are not normally distributed making the mean value and standard deviation less relevant for analysis. The metrics are

Table 3
Summary of the test results, comparing Test 1 and Test 2.

	Reference test set Test 1	Flight test set Test 2
<u>Depth back wall</u> ($x = 400\text{--}700$ mm)	Mode: 0.195 m, Median: 0.192 m p25 %: 0.190, p75 %: 0.198	Mode: 0.190 m, Median: 0.195 m p25 %: 0.190, p75 %: 0.201
<u>Depth delamination</u> ($x = 100\text{--}300$ mm $y = 200\text{--}700$ mm)	Mode: 0.145 m, Median: 0.149 m p25 %: 0.146, p75 %: 0.225	Mode: 0.110 m, Median: 0.209 m p25 %: 0.149, p75 %: 0.263
<u>Depth tendon duct</u> ($x = 800$ mm $y = 0\text{--}1000$ mm)	Mode: 0.275 m, Median: 0.279 m p25 %: 0.260, p75 %: 0.285	Mode: 0.270 m, Median: 0.282 m p25 %: 0.268, p75 %: 0.324
<u>Delamination Width</u>	200 mm	200 mm
<u>Delamination Length</u>	600 mm	600 mm
<u>Tendon Duct Width</u>	100 mm	100 mm
<u>Tendon Duct Length</u>	1100 mm	1100 mm

calculated for the B-C-D range protection that correspond to the coordinate range where a feature appears. The according coordinate range considered for these calculations is also mentioned in the table and can directly be used to calculate the width and length of the defects. The delamination and tendon duct width and length are estimated from the thickness profile. Hereby, it has to be considered that the accuracy is limited by the distance between the grid points. The values were calculated based on a sound velocity of 4030 m/s and by applying a filtering between 5 kHz and 20 kHz.

3.3. Flight testing with vertical measurements

This section presents the results of Test 3 containing preliminary flight testing on a concrete wall with vertical measurements. Fig. 18 illustrates measurement results of the drone system inspecting the concrete wall with four designated measurement points labeled p1 to p4. The drone maintains a horizontal pitch position during the inspection. An overlay is applied to the real structure, showing a color-coded thickness profile, providing a visual representation of the measured data. This overlay was created during post-processing in echolyst. Below

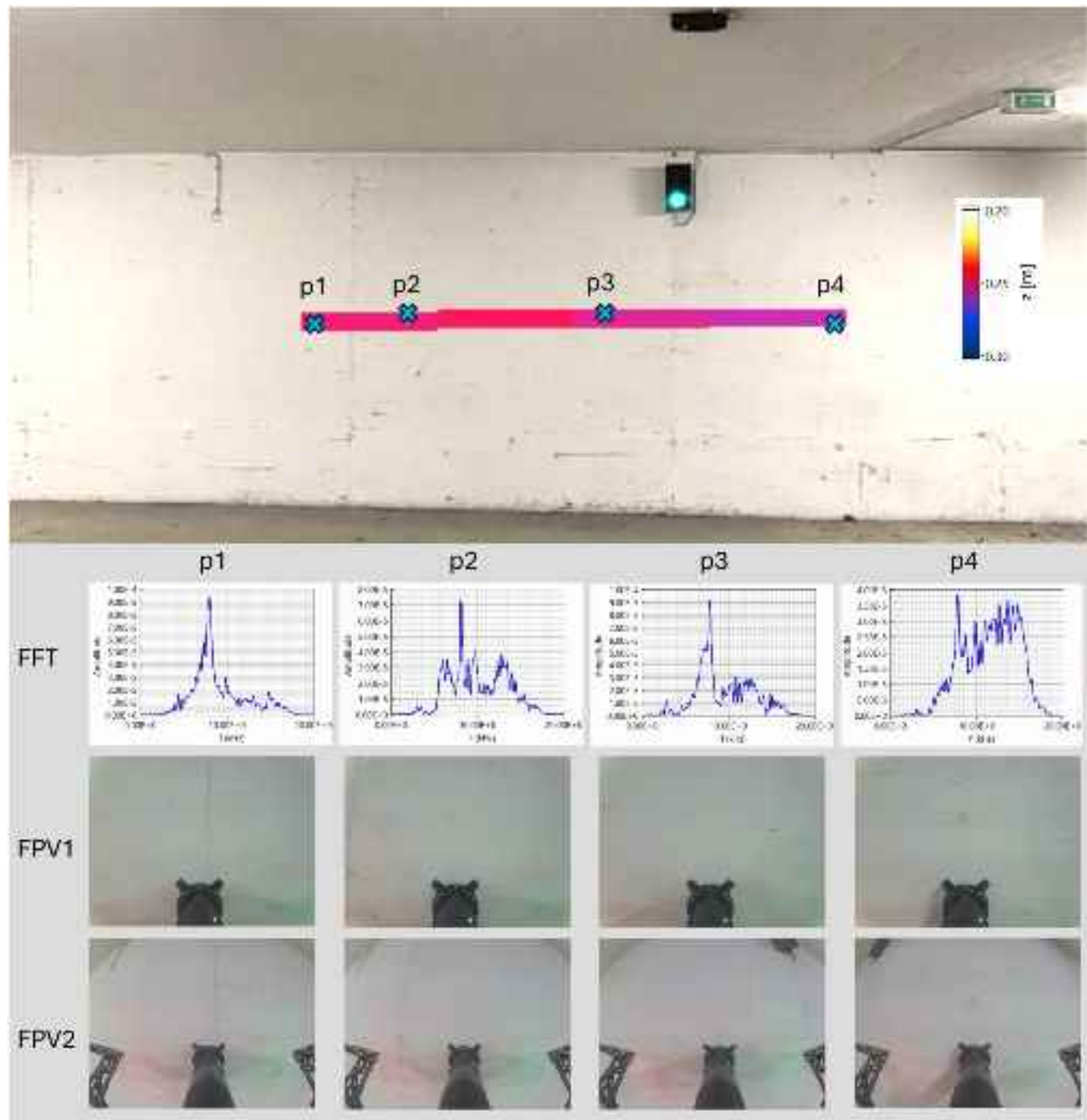


Fig. 18. Flight test results collected on the concrete wall, Test 3: visualization of the measurement results, including the overlay of the thickness profile on the real structure. Below, the FFT of the signals at each measurement location are displayed, providing detailed insight into the collected data. Additionally, two first-person view (FPV) images for each measurement point—one from a normal angle and one from a wide-angle perspective—aid in contextual understanding of the inspection environment.

the overlay image, the figure presents the respective Fast Fourier Transform (FFT) analyses for each signal after post-processing, giving insight into the dominant frequency components of the measurements that correlate with the wall thickness. In this example the gates for bandpass filtering are set to 3 kHz and 17 kHz. Additionally, two pictures of the first-person view (FPV) camera feeds from the drone are displayed which were captured during data collection for each measurement location: one picture displaying the normal angle (FPV1) and the other the wide-angle perspective (FPV2). The wall thickness measurement of the four points has a mean value of 24.3 cm with a standard deviation of 0.3 cm. This agrees very well with the reference values where we measured a mean value of 24.1 cm with a standard deviation of 0.2 cm.

This figure indicates the potential of the drone-based impact-echo system in combination with the data post-processing in echolyst and serves as an example of the expected results for practitioners, combining key elements such as:

- The overlay of the thickness profile on the real structure,
- The signals at each measurement location
- Two FPV images for each measurement point, aiding in contextual understanding.

The flight tests conducted on a real concrete wall successfully demonstrated the system's capabilities and potential for practical applications. Although a full measurement grid was beyond the scope of this initial proof-of-concept, the test focused on four measurement points arranged along a horizontal line in the middle of the wall. The results provide valuable insights into the system's performance. They show that the system effectively responds to varying surface conditions of a real concrete structure, maintaining reliable measurements. Additionally, the tests confirm the feasibility of obtaining meaningful thickness profiles and signal data with a limited set of measurement points, reinforcing the system's efficiency without the need for extensive scanning. Furthermore, the findings offer a practical perspective on how this approach can be implemented in future large-scale inspections, demonstrating its potential for real-world applications. Overall, these successful flight tests highlight the system's ability to deliver accurate and actionable data, marking an important step toward further development and deployment in real-world inspection scenarios.

4. Discussion of the results

In this study a new impact-echo sensor unit was developed that allows for drone-based impact-echo inspections. The sensor unit integrated into a drone research platform. This drone is able to apply contact forces at different pitch orientations while carrying the sensor unit weighing around 900 g. It was fully integrated in terms of mechanical, electronics, and software aspects, including wireless communication between the impact-echo system and the controller. The publication details the significant design effort in the signal acquisition pre-processing strategy. In particular, the specific routine implemented to pre-process the signals obtained from the drone-based impact-echo compared to traditional manual devices was described. The concept was tested and proofed by taking measurements on a concrete test block that contains known inspection targets, including a delamination and a tendon duct. The results of the drone-based system were compared with those from a reference measurement series obtained with a standard manual impact-echo device. Measurements were collected in a grid over the same area of the concrete block surface. The results were presented in C-projection and B-projection, providing, respectively, surface and cross-sectional image reconstruction of the inside of the concrete test block. These images were obtained by processing the individual spectrum response of the impact-echo signals. The singular dominant frequencies found for each element in the block were the same for the flight test and the reference test. This consistency confirmed the altered

impact-echo unit maintained its sensing abilities even under flying conditions. These results show that both the delamination as well as the tendon duct was successfully detected by the drone. Still, some results indicated that the repeatability of the coupling conditions and thus the robustness of the measurement can be further optimized.

5. Conclusions

The current paper presents a novel drone-based impact-echo concrete measurement system. The drone inspection system was able to detect and locate both the delamination as well as the tendon duct, which demonstrated the feasibility of the drone-based impact-echo concrete inspection system. This is a very promising result for future bridge and infrastructure inspections. These structures need to be inspected on a regular basis to find defects such as delaminations at an early stage prior to hazardous failure. Therefore, future research will address impact-echo measurements on bridge test sites. Exploiting the drone-based measurement system also on large infrastructure will also help to gain more experience and give insights to tailor the development regarding practicability. To target this and to further expand the system towards industrial applicability on real world structures, the system will be further developed according to the current results. Some results indicated that the repeatability of the coupling conditions and thus the robustness of the measurement can be further optimized. Therefore, the goal of future studies will be to improve the consistency of the coupling strengths between the sensor and the concrete surface. In future work, the effect of drone pitch and wind conditions on measurement quality will be quantified to assess their influence on impact precision and signal reliability. Additionally, future research could include further flight measurements on a denser grid.

The experiment detailed in this paper was executed using a test block exhibiting a reasonably representative model for concrete structures and implementing the impact-echo method. Nevertheless, a more extensive set of scenarios demands exploration to assess the drone-based inspection module under development comprehensively. Specifically, this entails including a broader spectrum of wall thicknesses and a comprehensive range of delamination sizes and depths. Given that the impact-echo method relies on a frequency domain analysis, the impact of rotor-induced vibrations generated during drone operation may vary for dissimilar wall thicknesses and resonance frequencies. Thus, this necessitates a thorough investigation.

Although the tests were carried out on flat horizontal surfaces exclusively up to this point, extending these assessments to encompass vertical surfaces and overhead positions is imperative. Furthermore, while numerous experiments will be performed on test specimens to enable precise parameter control, conducting tests on real-world structures is also crucial. This will provide invaluable insights into the testing environment and the associated specific challenges. Additionally, while the majority of tests will be executed on flat surfaces, curved surfaces present an additional challenge that requires a dedicated performance analysis. While the impact echo method is proven to work on curved surfaces such as in tunnel inspections, a strategic arrangement of the impactor and sensor in an axial rather than a circumferential direction could be considered and investigated to ensure good coupling. The drone platform has limited weight capacity for its payload, restricting the integration of heavier sensors or sensor arrays. To accommodate additional weight, the drone's design and specifications could be revised for enhanced payload capability in future research. Additionally research into design optimization leading to weight reduction of the impact-echo system will be considered in future works.

While the current work focuses on standard impact-echo and standard procedures to analyze the collected data, future work will also consider advanced data analysis techniques and machine learning algorithms to enable automated defect detection and classification. Machine learning approaches, such as convolutional neural networks (CNNs) and anomaly detection algorithms, will be explored to enhance

pattern recognition and classification capabilities. Additionally, real-time data processing and adaptive learning techniques will be integrated to improve system responsiveness and reliability. This effort will contribute to more efficient quality control processes and reduced inspection times, ultimately enhancing overall system performance and productivity.

In the long term, it can be concluded that the developed flying impact-echo system has the potential to be used for future bridge inspections and infrastructure assessments at height. Once deployed, this technology will significantly improve the diagnostics and maintenance of infrastructure, which will contribute to improved sustainability and resilience. Furthermore, the inspection system also has the ability to achieve faster and more robust concrete inspections as it does not require measurement support structures such as cherrypickers, and measurements can be taken very efficiently during flight. Also, the repeatability is generally higher by utilizing robotized systems. Finally, the inspection could even be further accelerated by implementing a flight controller that is able to collect the signals automatically according to a pre-defined flight path.

CRediT authorship contribution statement

Algernon Daniel: Writing – review & editing, Visualization, Supervision, Software, Funding acquisition, Formal analysis, Conceptualization. **Muller Aurélia:** Writing – review & editing, Methodology. **Thurnherr Claudia:** Writing – original draft, Visualization, Validation, Software, Project administration, Methodology, Investigation, Formal analysis, Data curation, Conceptualization.

Declaration of Competing Interest

The authors declare that they have no known competing financial interests or personal relationships that could have appeared to influence the work reported in this paper.

Acknowledgments

The authors gratefully acknowledge the support of Nicolas Scheidt (Voliro AG) during the technical implementation of the integration to the drone computer. Furthermore, the authors would like to sincerely thank Leonardo Rössler (SVTI) for his support during the 3D design phase as well as during the testing.

Data availability

Data will be made available on request.

References

- [1] A. Albers, S. Trautmann, T. Howard, T.A. Nguyen, M. Frietsch, C. Sauter, 2010. Robotics, automation, and mechatronics (RAM), In: Proceedings of the 2010 IEEE Conference on: date, 28-30 June 2010. 2010 IEEE Conference on Robotics, Automation and Mechatronics, pp. 441–446..
- [2] D. Algernon, S. Feistkorn, M. Hagenbruch, P. Kicherer, L. Rössler, M. Scherrer, 2021. ECHOLYST - Entwicklung eines Impact-Echo-Systems für Scanning, Analyse und Machine Learning. (<http://www.ndt.net/?id=25759>).
- [3] J.-P. Balayssac, V. Garnier, Non-Destructive Testing and Evaluation of Civil Engineering Structures, Elsevier, 2017.
- [4] K. Bodie, M. Brunner, M. Pantic, S. Walser, P. Pfändler, U. Angst, R. Siegwart, J. Nieto, 2019. An omnidirectional aerial manipulation platform for contact-based inspection. ArXiv Preprint ArXiv:1905.03502..
- [5] R. Bogue, Applications of robotics in test and inspection, Ind. Robot.: Int. J. 45 (2) (2018) 169–174, <https://doi.org/10.1108/IR-01-2018-0012>.
- [6] P. Candeloro, D. Ragni, T. Pagliaroli, Small-scale rotor aeroacoustics for drone propulsion: a review of noise sources and control strategies, Fluids 7 (8) (2022) 279, <https://doi.org/10.3390/FLUIDS7080279>.
- [7] C. Cheng, M. Sansalone, The impact-echo response of concrete plates containing delaminations: numerical, experimental and field studies, Mater. Struct. 26 (5) (1993) 274–285.
- [8] G.G. Clemeña, & others. 1995. Use of the impact-echo method in nondestructive measurements of the thickness of new concrete pavements..
- [9] DGZfP. 2021. MERKBLATT B 11 Merkblatt über die Anwendung des Impakt-Echo-Verfahrens zur Zerstörungsfreien Prüfung von Betonbauteilen.
- [10] S. Feroz, S.A. Dabous, UAV-based remote sensing applications for bridge condition assessment, Remote Sens. 13 (9) (2021) 1809, <https://doi.org/10.3390/RS13091809>.
- [11] J. Fu, G. Liu, C. Fan, Z. Liu, H. Luo, Design and experimental study on vibration reduction of an UAV lidar using rubber material, Actuators 11 (12) (2022) 345, <https://doi.org/10.3390/ACT11120345>.
- [12] Patrick Gaydecki, 2004, Foundations of digital signal processing: theory, algorithms and hardware design, 462..
- [13] R.S. Geronel, D.D. Bueno, Adaptive sliding mode control for vibration reduction on UAV carrying a payload, J. Vib. Control (2025), <https://doi.org/10.1177/10775463241231845>.
- [14] A. Gibson, J.S. Popovics, Lamb wave basis for impact-echo method analysis, J. Eng. Mech. 131 (4) (2005) 438–443, [https://doi.org/10.1061/\(ASCE\)0733-9399\(2005\)131:4\(438\)](https://doi.org/10.1061/(ASCE)0733-9399(2005)131:4(438)).
- [15] L.M. González-deSantos, J. Martínez-Sánchez, H. González-Jorge, F. Navarro-Medina, P. Arias, UAV payload with collision mitigation for contact inspection, Autom. Constr. 115 (2020) 103200, <https://doi.org/10.1016/J.AUTCON.2020.103200>.
- [16] L.M. González-Desantos, J. Martínez-Sánchez, H. González-Jorge, M. Ribeiro, J. B. de Sousa, P. Arias, Payload for contact inspection tasks with UAV systems, Sensors 19 (17) (2019), <https://doi.org/10.3390/S19173752>.
- [17] R. Helmerich, E. Niederleitinger, D. Algernon, D. Streicher, H. Wiggenhauser, Bridge inspection and condition assessment in europe, Transp. Res. Rec. 2044 (2008) 31–38, <https://doi.org/10.3141/2044-04>.
- [18] B.J. Jaeger, M.J. Sansalone, R.W. Poston, Detecting voids in grouted tendon ducts of post-tensioned concrete structures using the impact-echo method, Struct. J. 93 (4) (1996) 462–473.
- [19] Kamel, M. 2019. Physical interaction with micro aerial vehicles: control and design [DISS. ETH NO. 26031]. ETH Zurich.
- [20] M. Kamel, S. Verling, O. Elkhatib, C. Sprecher, P. Wulkop, Z. Taylor, R. Siegwart, I. Gilitschenski, The voliro omniorientational hexacopter: an agile and maneuverable tiltable-rotor aerial vehicle, IEEE Robot. Autom. Mag. 25 (4) (2018) 34–44, <https://doi.org/10.1109/MRA.2018.2866758>.
- [21] Y.T. Ke, Y.C. Lin, C.C. Cheng, J.C. Chen, Y.H. Pai, K.T. Hsu, Preliminary study on defect detection for sandwich composites using Impact-Echo method, Int. J. Appl. Sci. Eng. 20 (2) (2023), [https://doi.org/10.6703/IJASE.202306.20\(2\).002](https://doi.org/10.6703/IJASE.202306.20(2).002).
- [22] S.-H. Kee, N. Gucunski, Interpretation of flexural vibration modes from impact-echo testing, J. Infrastruct. Syst. 22 (3) (2016), [https://doi.org/10.1061/\(ASCE\)1943-555X.0000291](https://doi.org/10.1061/(ASCE)1943-555X.0000291).
- [23] I.H. Kim, S. Yoon, J.H. Lee, S. Jung, S. Cho, H.J. Jung, A comparative study of bridge inspection and condition assessment between manpower and a UAS, Drones 6 (11) (2022) 355, <https://doi.org/10.3390/DRONES6110355>.
- [24] K. Kondak, A. Ollero, I. Maza, K. Krieger, A. Albu-Schaeffer, M. Schwarzbach, M. LaickerUnmanned Aerial Systems Physically Interacting with the Environment. Load Transportation, Deployment and Aerial Manipulation. In Handbook of unmanned aerial vehicles pp. 2755–27852015.
- [25] A. Kumar, B. Raj, P. Kalyanasundaram, T. Jayakumar, M. Thavasiuthu, Structural integrity assessment of the containment structure of a pressurised heavy water nuclear reactor using impact echo technique q, NDTE Int. 35 (2002) 213–220. (www.elsevier.com/locate/ndteint).
- [26] Z. Li, M. Lao, S.K. Phang, M. Redhwan, A. Hamid, K. Zuea Tang, F. LinDevelopment and design methodology of an anti-vibration system on micro-UAVs. In: Proceedings of the International Micro Air Vehicle Conference and Flight Competition (IMAV) 2017, 223–228. <http://www.imavs.org/pdf/imav.2017.322017>.
- [27] Q. Lindsey, D. Mellinger, V. Kumar, Construction of cubic structures with quadrotor teams, Proc. Robot.: Sci. Syst. 7 (2011).
- [28] C. Maierhofer, G. Zacher, C. Kohl, J. Wöstmann, Evaluation of radar and complementary echo methods for NDT of concrete elements, J. Nondestruct. Eval. 27 (1–3) (2008) 47–57, <https://doi.org/10.1007/S10921-008-0030-8/METRICS>.
- [29] Christiane Maierhofer, H.-Wolf Reinhardt, Gerd Dobmann, Non-Destructive Evaluation of Reinforced Concrete Structures. Volume 1, Deterioration Processes and Standard Test Methods, CRC Press, 2010.
- [30] N. Michael, J. Fink, V. Kumar, Cooperative manipulation and transportation with aerial robots, Auton. Robots 30 (2011) 73–86.
- [31] M. Momayez, F.P. Hassani, P. Guevremont, K. Saleh, S. Tremblay, An investigation of the MSR Impact-echo method for concrete dam inspection, Hydro-Rev. Pap. (2001).
- [32] M. Morales-Rodriguez, P. Chen, P. Fuhr, S. Rooke, Drones in automation, InTech, Int. Soc. Autom. (2017).
- [33] A.M. Muller, C. Thurnherr, D. Algernon, Intégration d'un système CND Impact Echo sur un drone, E-J. Nondestruct. Test. 28 (9) (2023), <https://doi.org/10.5828/28518>.
- [34] P. Nooralishahi, C. Ibarra-Castanedo, S. Deane, F. López, S. Pant, M. Genest, N. P. Avdelidis, X.P.V. Maldague, Drone-based non-destructive inspection of industrial sites: a review and case studies, Drones 5 (4) (2021) 106, <https://doi.org/10.3390/drones5040106>.
- [35] A. Ollero, J. Cortes, A. Santamaría-Navarro, M.A. Trujillo Soto, R. Balachandran, J. Andrade-Cetto, A. Rodriguez, G. Heredia, A. Franchi, G. Antonelli, K. Kondak, A. Sanfelix, A. Viguria, J.R. Martinez-de Dios, F. Pierri, The AEROARMS project: aerial robots with advanced manipulation capabilities for inspection and maintenance, IEEE Robot. Autom. Mag. 25 (4) (2018) 12–23, <https://doi.org/10.1109/MRA.2018.2852789>.

- [36] Pfändler, P., Bodie, K., Angst, U., & Siegwart, R. (2019). Flying corrosion inspection robot for corrosion monitoring of civil structures—First results. In SMAR 2019-Fifth Conference on Smart Monitoring, Assessment and Rehabilitation of Civil Structures-Program (pp. We-4). SMAR.
- [37] PortAudio Documentation. 2020. (<http://www.portaudio.com>) 2020.
- [38] M. Rucka, E. Wojtczak, M. Zielińska, Integrated application of GPR and ultrasonic testing in the diagnostics of a historical floor, *Materials* 13 (11) (2020) 2547, <https://doi.org/10.3390/MA13112547>.
- [39] M. Ryll, G. Muscio, F. Pierri, E. Cataldi, G. Antonelli, F. Caccavale, A. Franchi6D physical interaction with a fully actuated aerial robot. In: Proceedings of the 2017 IEEE International Conference on Robotics & Automation. <http://ieeexplore.ieee.org/>2017.
- [40] M. Sansalone, N.J. Carino, Impact-echo: a method for flaw detection in concrete using transient stress waves, *U. S. Dep. Commer., Natl. Inst. Stand. Technol. (1986)*.
- [41] Sansalone, M.J., & Streett, W.B. 1997. Impact-echo. Nondestructive evaluation of concrete and masonry.
- [42] Y.H. Shin, D. Kim, S. Son, J.W. Ham, K.Y. Oh, Vibration isolation of a surveillance system equipped in a drone with mode decoupling, *Appl. Sci.* 11 (4) (2021) 1961, <https://doi.org/10.3390/APP11041961>.
- [43] N. Staub, D. Bicego, Q. Sablé, V. Arellano-Quintana, S. Mishra, A. Franchi, V. Arellano, 2018. Towards a flying assistant paradigm: the OTHexIn: Proceedings of the IEEE International Conference on Robotics & Automation. (<http://ieeexplore.ieee.org/>).
- [44] C. Thurnherr, A. Müller, L. Rössler, D. Algernon, 2022. Uncrewed aerial concrete inspection system. In: Proceedings of the International Symposium on Non-Destructive Testing in Civil Engineering (NDT-CE) (Ed.), .
- [45] Y. Tinkey, L.D. Olson, Impact-echo scanning for grout void detection in post-tensioned bridge ducts-findings from a research project and a case history, *ASCE Struct. Congr.* (2007).
- [46] Y. Tinkey, L.D. Olson, H. Wiggenhauser, Impact echo scanning for discontinuity detection and imaging in posttensioned concrete bridges and other structures, *Mater. Eval.* 63 (1) (2005).
- [47] G. Vasiljevic, D. Martinovic, M. Orsag, S. BogdanGrabbing power line conductors based on the measurements of the magnetic field strength. In: Proceedings of the 2021 Aerial Robotic Systems Physically Interacting with the Environment (AIRPHARO), pp. 1–7. <https://doi.org/10.1109/AIRPHARO52252.2021.9571037>2021.
- [48] M. Verma, C. ColletteActive vibration isolation system for drone cameras. In: Proceedings of the 14th International Conference on Vibration Problems: ICOVP 2019., 58, 1067–1084. https://doi.org/10.1007/978-981-15-8049-9_672021.
- [49] R.J. Watson, S.G. Pierce, M. Kamel, D. Zhang, C.N. MacLeod, G. Dobie, G. Bolton, T. Dawood, J. Nieto, 2021, Deployment of contact-based ultrasonic thickness measurements using over-actuated UAVs. pp. 683–694. https://doi.org/10.1007/978-3-030-64594-6_66.
- [50] H. WiggenhauserDuct inspection using scanning impact-echo. In: Proceedings of International Symposium NDT-CE 2003, Tendon Ducts.2003.
- [51] J. Zhu, J.S. Popovics, M. Asce, Imaging concrete structures using air-coupled impact-echo, *J. Eng. Mech.* 133 (6) (2007) 628–640, <https://doi.org/10.1061/ASCE0733-93992007133:6628>.